



Spatio-temporal characteristics of small-scale wave–current ripples on the Ameland ebb-tidal delta

Laura Brakenhoff,* Maarten Kleinhans, Gerben Ruessink and Maarten van der Vegt

Department of Physical Geography, Faculty of Geosciences, Utrecht University, Utrecht, The Netherlands

Received 16 July 2019; Revised 16 December 2019; Accepted 17 December 2019

*Correspondence to: Laura Brakenhoff, Department of Physical Geography, Faculty of Geosciences, Utrecht University, PO Box 80115, 3508 TC Utrecht, The Netherlands. E-mail: L.b.brakenhoff@uu.nl

This is an open access article under the terms of the Creative Commons Attribution License, which permits use, distribution and reproduction in any medium, provided the original work is properly cited.

ESPL

Earth Surface Processes and Landforms

ABSTRACT: Ebb-tidal deltas are highly dynamic environments affected by both waves and currents that approach the coast under various angles. Among other bedforms of various scales, these hydrodynamics create small-scale bedforms (ripples), which increase the bed roughness and will therefore affect hydrodynamics and sediment transport. In morphodynamic models, sediment transport predictions depend on the roughness height, but the accuracy of these predictors has not been tested for field conditions with strongly mixed (wave–current dominated) forcing. In this study, small-scale bedforms were observed in the field with a 3D Profiling Sonar at five locations on the Ameland ebb-tidal delta, the Netherlands. Hydrodynamic conditions ranged from wave dominated to current dominated, but were mixed most of the time. Small-scale ripples were found on all studied parts of the delta, superimposed on megaripples. Even though a large range of hydrodynamic conditions was encountered, the spatio-temporal variations in small-scale ripple dimensions were relatively small (height $\eta \approx 0.015$ m, length $\lambda \approx 0.11$ m). Also, the ripples were always highly three-dimensional. These small dimensions are probably caused by the fact that the bed consists of relatively fine sediment. Five bedform height predictors were tested, but they all overestimated the ripple heights, partly because they were not created for small grain sizes. Furthermore, the predictors all have a strong dependence on wave- and current-related velocities, whereas the ripple heights measured here were only related to the near-bed orbital velocity. Therefore, ripple heights and lengths in wave–current-dominated, fine-grained coastal areas ($D_{50} < 0.25$ mm) may be best estimated by constant values rather than values dependent on the hydrodynamics. In the case of the Ameland ebb-tidal delta, these values were found to be $\eta = 0.015$ m and $\lambda = 0.11$ m. ©2019 The Authors. Earth Surface Processes and Landforms published by John Wiley & Sons Ltd.

KEYWORDS: sonar; bedform predictors; wave–current ripples; three-dimensionality; fine sand

INTRODUCTION

Ebb-tidal deltas are subtidal bodies of sand located seaward of tidal inlets, which makes them subject to both waves and cross-shore and longshore currents. Interaction between these hydrodynamics and the sandy bed creates bedforms on a variety of scales. The largest bedforms on ebb-tidal deltas are sandy shoals, which have been studied thoroughly by, for example, FitzGerald (1982) and Ridderinkhof *et al.* (2016). In the Wadden Sea region, saw-tooth bars are often present on the downdrift side of ebb-tidal deltas, with heights up to 2 m and wavelengths (i.e. spacings) of about 700 m (Brakenhoff *et al.*, 2019). The characteristics of smaller bedforms on ebb-tidal deltas, like ripples and megaripples, are less well studied, despite their relevance for sediment transport.

Megaripples (or dunes) are defined as bedforms with height $\eta > 0.1$ m and wavelength $\lambda > 0.6$ m (Ashley, 1990), while small-scale ripples have η of the order of centimetres and $\lambda < 1$ m (Jackson, 1975). Previous studies have focused on megaripples and other similarly scaled bedforms in the

current-dominated channels and tidal inlets (e.g. Buijsman and Ridderinkhof, 2008) or on the more wave-dominated intertidal shoals (Hoekstra *et al.*, 2004). Passchier and Kleinhans (2005) observed three-dimensional megaripples on the Dutch continental shelf in 14–18 m water depth when the current- and wave-related Shields numbers were both above 0.1.

Small-scale wave–current ripples have not been studied for the mixed forcing conditions of ebb-tidal deltas either. Studies do exist on wave–current ripples in shallow water along straight coasts or on nearshore bars (e.g. Meirrelles *et al.*, 2016; Wengrove *et al.*, 2018; Wu and Parsons, 2019) and on continental shelves (e.g. Li and Amos, 1999; Krämer and Winter, 2016). In most cases, rather two-dimensional ripples were observed, but that might be caused by either the constant angle between waves and currents, or by the fact that, although waves and currents were both present, one of the two was still clearly dominant. In flume studies it was found that it is possible for ripples to become three-dimensional when waves and currents are perpendicular to each other

(Andersen and Faraci, 2003). Li and Amos (1999) even found three-dimensional ripples when the angle between waves and currents was 30°. Yet it is unclear how these flume studies relate to the dynamic conditions of ebb-tidal deltas.

Bedforms like ripples affect both hydrodynamics and sediment transport. They create additional bed roughness on top of the grain-related roughness, which affects the vertical mixing in the flow (Smith and McLean, 1977; Nielsen, 1979; Lefebvre *et al.*, 2013, 2014). Models that are used to estimate sediment transport, like Delft3D, TELEMAC and MIKE21, are dependent on roughness predictors to calculate sediment transport (Tonnon *et al.*, 2007; Elias and Hansen, 2013; Herrling and Winter, 2014; Lenstra *et al.*, 2019; McCann *et al.*, 2011; Deigaard *et al.*, 1999). This means that it is important to correctly predict the presence and height of the bedforms. The bedform roughness height predictor of van Rijn (2007) is incorporated into the frequently used model Delft3D, Tanaka and Dang (1996) is incorporated into TELEMAC and MIKE21 uses Nielsen (1979).

For a predictor to correctly represent the mixed hydrodynamic situation of ebb-tidal deltas, it should incorporate both waves and currents. Predictors that meet this condition include Tanaka and Shuto (1984), Tanaka and Dang (1996), Khelifa and Ouellet (2000) and van Rijn (2007). However, Tanaka and Shuto (1984) and Tanaka and Dang (1996) were created for the specific condition in which waves and currents are opposing each other (180° difference in direction). Khelifa and Ouellet (2000) do account for all possible angles, but the predictor was only tested for laboratory conditions. Furthermore, both Khelifa and Ouellet (2000) and van Rijn (2007) calculate the equilibrium height of the bedforms. Because of the highly variable hydrodynamic conditions on ebb-tidal deltas, it can be questioned whether this equilibrium height will ever be reached.

Various recent studies show that it is important to incorporate time-dependent aspects into the calculation of bedform height, including the previous bed state (e.g. Davis *et al.*, 2004; Nelson and Voulgaris, 2014; Soulsby *et al.*, 2012; Traykovski, 2007). Soulsby *et al.* (2012) is the only predictor that incorporates both waves and currents and the

time-variance. Wengrove *et al.* (2018) tested the (Soulsby *et al.*, 2012) predictor in shallow water (1–3 m) and found an r^2 of 0.55 for predicted ripple heights. Soulsby *et al.* (2012) tested their predictor in the field under 7 m deep continental shelf conditions, and found that 88% of the predicted ripple heights were within a factor of 2 of the measured ripple heights. This is higher than all predictors tested by Camenen (2009), although he studied only wave ripples and did not test the predictors mentioned above. So far, none of the predictive formulas for bedform geometry have been tested for the wave–current-dominated conditions on ebb-tidal deltas.

The main goal of this study is to better understand the characteristics of small-scale wave–current-dominated ripples. Therefore, their height, length and three-dimensionality were measured on an ebb-tidal delta (Ameland, the Netherlands), during a large range of hydrodynamic conditions. In this paper, the ripple characteristics are analysed and related to the hydrodynamic forcing. The measured ripple heights are also compared to those estimated with predictors used in models such as Delft3D, TELEMAC and MIKE21.

DATA AND METHODS

Study site

The ebb-tidal delta of the Ameland Inlet, which is located in the Dutch part of the Wadden Sea, was chosen as the study site, as it is regarded as the least disturbed inlet in the Netherlands (Elias *et al.*, 2012). The Ameland inlet alternates between a two-channel and a single-channel configuration (Israel and Dunsbergen, 1999). Currently, two channels are present but one is clearly dominant (Figure 1). The delta itself consists of two lobes – one in the east and one in the west – with minimum water depths of approximately 1 m relative to mean sea level. It is subjected to wind-generated waves approaching mainly from the northwest (Figure 1), with an average significant height H_s of 1.3 m, and an average spectral period T_{m01} of 5 s (Roskam, 1988). Maximum significant storm wave heights can be more than 6 m, with storm surges of over 2 m. The tidal

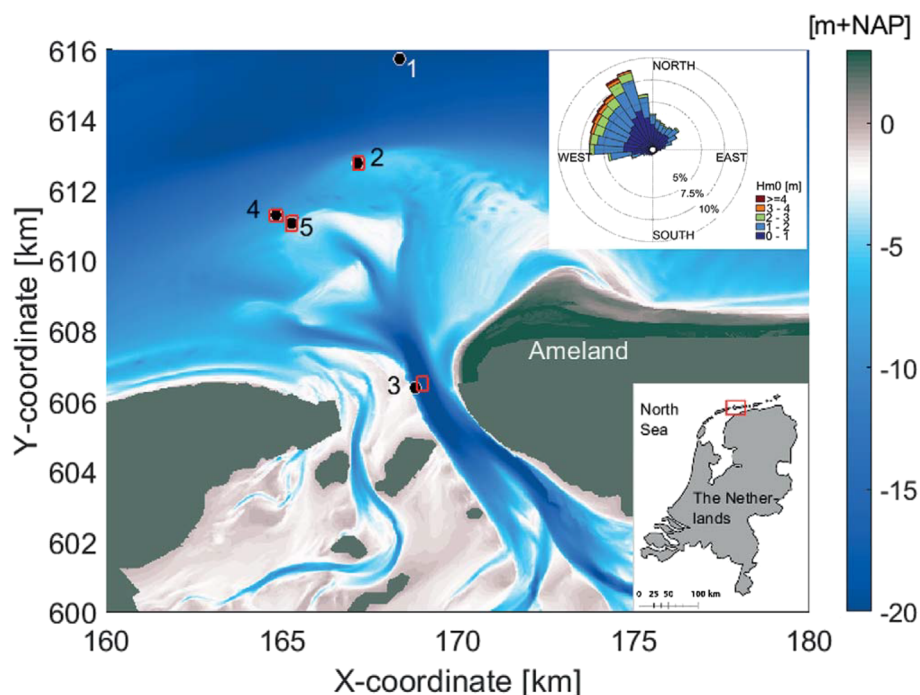


Figure 1. Bathymetry of the Ameland ebb-tidal delta of 2017 (measured by Rijkswaterstaat), including the locations of multibeam measurements (red squares) and measurement frames (black dots). A wave rose is plotted at the upper right, showing the wave climate between 1996 and 2019 at an offshore wavebuoy located approximately 40 km northeast of the study site [Colour figure can be viewed at wileyonlinelibrary.com]

wave propagates along the coast from west to east, and near Ameland the tidal range is ~ 2 m. Maximum shore-parallel velocities are $0.5\text{--}1.0\text{ m s}^{-1}$ (Elias *et al.*, 2012), and the tidal prism is 430 Mm^3 (Sha, 1989). Across the entire ebb-tidal delta, the mean grain size (D_{50}) is 0.211 mm , with a standard deviation of 0.03 mm and a mud content ($<0.063\text{ mm}$) of 1% by volume (Pearson *et al.*, 2019).

Campaign

Small-scale ripples and hydrodynamics were studied with measurement frames offshore (frame 1), in the inlet throat (frame 3) and on three parts of the ebb delta lobe (frames 2, 4 and 5) (Figure 1). A sketch and a photo of one of the frames are given in Figure 2. The water depths at which the frames were deployed can be found in Table I. Frames 2–5 were deployed

between 29 August and 10 October 2017, and frame 1 was deployed between 8 November and 11 December 2017. To obtain an impression of the large-scale megaripples that could not be captured by the frames, areas of $500 \times 500\text{ m}$ around frames 2–5 were mapped with a multibeam echo-sounder before and after the campaign. The exact mapping dates are given in Table I. As visible in Figure 1, frame 3 was placed outside of the multibeam area, but the multibeam data of this area are assumed to be representative of the frame location as well. Before the field campaign, megaripples were present at all measured sites (Figure 3). Visually, near frames 2 and 3, they were quite regular, with heights of $0.3\text{--}0.4\text{ m}$ and lengths of the order of 10 m . Frames 4 and 5 were located in an area with more irregular megaripples, which had smaller heights ($\sim 0.1\text{ m}$) and larger wavelengths ($\sim 20\text{ m}$). After the

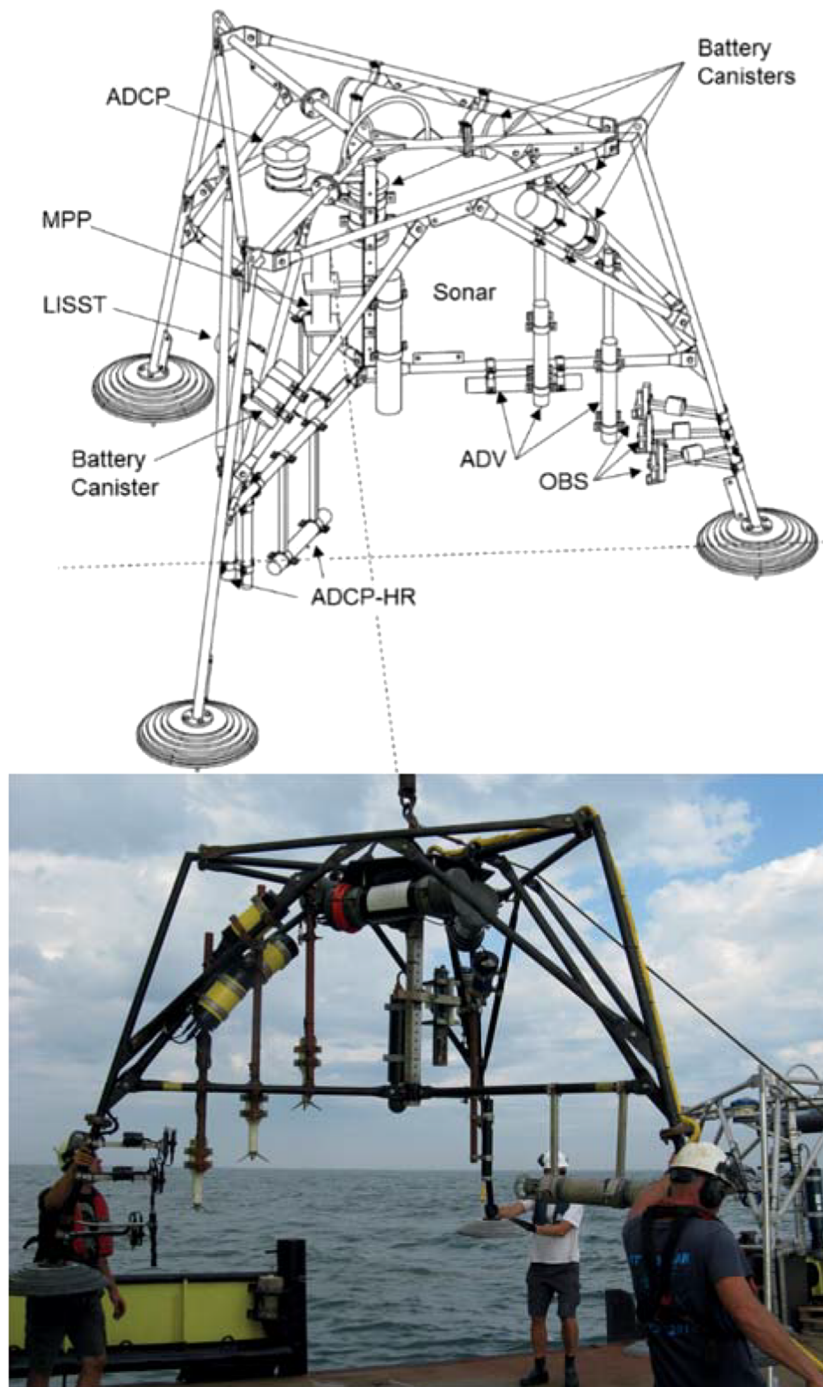
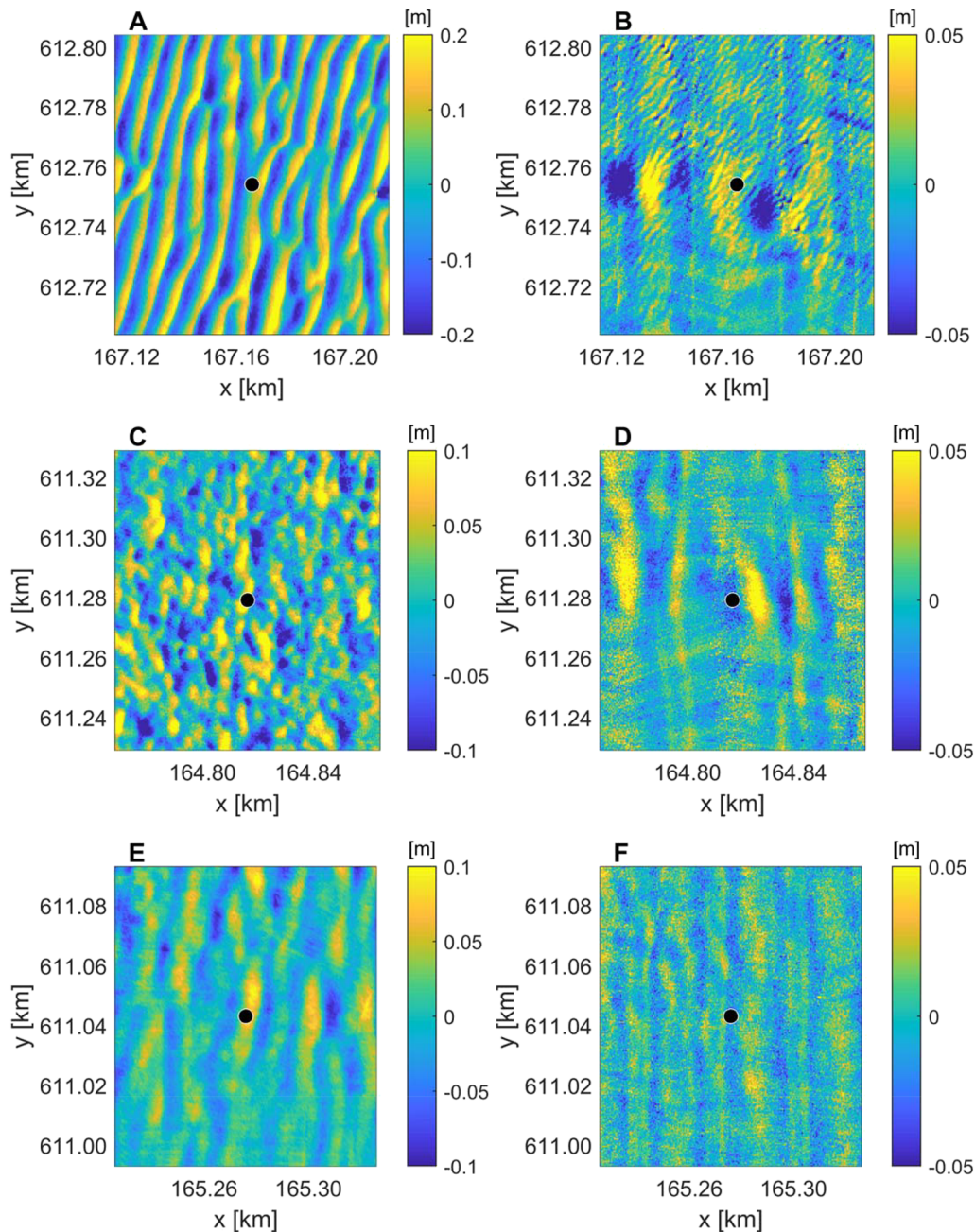


Figure 2. Sketch (top) and photo (bottom) of one of the five measurement frames [Colour figure can be viewed at wileyonlinelibrary.com]

Table 1. Average water depths and grain sizes at the measurement sites, and the dates of frame deployment and multibeam echo sounding (MBES)

Frame	Depth (m)	D50 (mm)	Frame deployment (dd-mm in 2017)	MBES survey dates (dd-mm in 2017)
1	20.4	0.226	08-11 to 11-12	—
2	8.6	0.225	30-08 to 09-10	29-08, 18-10
3	15.1	0.216	30-08 to 10-10	29-08, 15-11
4	8.9	0.186	29-08 to 09-10	29-08, 24-10
5	6.5	0.186	29-08 to 10-10	29-08, 24-10

**Figure 3.** Bed state around frames 2, 4 and 5 before (A, C, E) and after (B, D, F) the field campaign. Measurement frames are indicated with black dots. All plots are 100 × 100 m. The vertical lines in plots B, D and F are measurement artefacts of the multibeam swaths, which could not be corrected [Colour figure can be viewed at wileyonlinelibrary.com]

field campaign, the megaripples at frames 2, 4 and 5 had largely disappeared; at frame 2 the height decreased to 0.05 m. Near frame 3, however, the megaripple heights and lengths were the same before and after the field campaign.

Equipment

All frames were equipped with a Marine Electronics type 2001 3D Profiling Sonar, mounted at approximately 0.9 m above the bed to obtain regular maps of small-scale bedforms beneath the frame. It was set to scan the bed once per hour, rotat-

ing around its own axis, which took approximately 15 min. Each scan consisted of 200 swaths of the bed in a 360° circle; thus all swaths were 0.9° apart. The maximum deviation of the sonar beam was 75° from the vertical. A single swath contained 166 vertical backscatter profiles, so the profiles were spaced 0.9° apart. Each profile consisted of 842 samples between 0 and 3.7845 m from the sonar head, so the vertical resolution (in the direction of the beam) was approximately 4.5 mm. The horizontal resolution for each swath was smallest right below the sonar head (0.016 m) and increased to 0.22 m at the edges of the swath (>3.5 m away from the centre of the image). To prevent resolution issues in studying small-scale ripples, only the inner part of the scanned sea bed – a circle with a radius of 1 m – was used here, which gave a maximum horizontal spacing between measurements of 0.03 m.

Each frame also contained two acoustic Doppler velocity meters (ADV) to measure wave- and current-related velocities and directions. Their measurement volumes were located approximately 0.35 and 0.65 m above the bed. Frames 4 and 5 contained an extra ADV at 1 m above the bed. The ADVs at frames 1–4 (Nortek Vector) sampled continuously at 16 Hz, whereas the ADVs at frame 5 (Sontek Hydra) sampled continuously at 10 Hz. On frames 1–4 a pressure transducer was incorporated into each ADV, and on frame 5 a separate pressure transducer was used, sampling continuously with a measurement frequency of 4 Hz. With these transducers, water depth, wave height and wave period were measured. The ADVs at frame 3 were subject to technical issues and most hydrodynamic data are missing for this frame. As visible in Figure 2, the frames were set up with the batteries on top, to disturb the flow near the bed and around the instruments as little as possible. Even though the space in between the frames' legs was maximized, it is unknown to what extent the flow was still disturbed.

Grain sizes near the frames were determined through box core samples (Table I). The sediment was found to be relatively fine, with grain sizes between 0.185 and 0.226 mm. More information about the field campaign and measurement equipment can be found in van der Vegt *et al.* (2020).

Data processing and analysis

The sonar images were processed using the bed detection method described by Ruessink *et al.* (2015). First, the bed was detected by a second-order polynomial smoothing of 11 data points around the point with maximum backscatter in each profile. Subsequently, a second-order scale-controlled filter (Plant *et al.*, 2002) was used to interpolate the detected bed points on to a regular 2 × 2 m grid with cells of 0.01 × 0.01 m. The adopted filter scale ensured that 70% or more of the variance of bed features with a length scale smaller than 0.05 m is removed. The mean distance to the sonar head was also removed from the bed elevation values, so that ripples are visible as perturbations. Positive values are the crests and negative values are the troughs. It was found that the frames' legs cause considerable scour; holes developed with a diameter of approximately 1 m and depth of 0.1 m. To remove the scour holes the perturbation maps were detrended with a third-order surface fit.

The orientation of the sonar is known with respect to the orientation of the other sensors. Given their heading, the sonar perturbation maps were rotated to the N-E-S-W scheme. After that, the quality of each image was assessed based on a visual inspection. Images in which the bed level clearly changed during the sonar rotation, and in which the bed could not be found because of a high amount of sediment in suspension,

were removed from the data set. From the remaining images, the ripple height η_m was calculated from $2\sqrt{2}\sigma$ (Krämer and Winter, 2016), with σ being the standard deviation of the image. Each image was then rotated in a full circle with steps of 5° and for each rotation the bedform three-dimensionality (Tb) was calculated using the autocorrelation of the bed elevation data in the x and y direction according to Núñez-González *et al.* (2014). Tb is a dimensionless parameter, ranging from 0 (indicating a purely two-dimensional bedform) to 1 (indicating a purely three-dimensional bedform). The rotation angle that resulted in the lowest value of Tb was taken to be the orientation of the ripples, although for highly three-dimensional bedforms this orientation is arbitrary. Using this orientation angle, ripple lengths (λ) were calculated by a wavelet, using the method of Grinsted *et al.* (2004), which was based on Torrence and Compo (1998). To obtain the dominant ripple length, the wavelength with the maximum power was calculated for each grid row, and then the median of all these wavelengths was taken to be the 'dominant' ripple length.

Current speeds in east–west (u) and north–south (v) directions were computed from the ADV data as 30 min average values. Total speed U was then given by $\sqrt{u^2 + v^2}$. The depth-averaged current velocity u_c was calculated from U using a logarithmic velocity profile on the lowest two available ADVs. This was validated by Nayak *et al.* (2015), who found that, even though the combination of waves and currents affects the roughness layer, the log layer is not much affected. The roughness layer is approximately twice the roughness element height (Florens *et al.*, 2013), which is in our case a few centimetres. Our ADVs were mounted at 0.35 and 0.65 m above the bed, which is well outside the roughness layer. Current directions were calculated using the Pythagorean theorem on u and v . The mean wave angle was also calculated from the ADV data, by a principal component analysis of the instantaneous high-frequency ($0.05 < f < 1$ Hz) velocities per 30 min.

The pressure sensors were used to calculate water depth h , significant wave height H_s and spectral wave period T_{m-10} . First, the data were divided into blocks of 30 min and linear wave theory was used to convert pressure to sea surface elevation. h was obtained by averaging the water depths in each block. H_s was calculated as $4\sqrt{m_0}$, where m_0 is the zero-order spectral moment of the high frequencies ($0.05 < f < 1$ Hz) in the sea surface elevation. The spectral wave period T_{m-10} was computed using the ratio of the moments m_{-1}/m_0 . For consistency with the methods of numerical models, the amplitude of near-bed orbital motion u_w was calculated according to linear theory with $\pi H_s/T_{m-10} \sinh(kh)$, in which k was approximated using the method of Guo (2002) with T_{m-10} and h . Wave- and current-related Shields parameters were calculated according to Kleinhans and Grasmeijer (2006):

$$\theta_x = \frac{\tau_x}{(\rho_s - \rho_w)gD50} \quad (1)$$

In this equation, $\rho_s = 2650 \text{ kg m}^{-3}$ and $\rho_w = 1025 \text{ kg m}^{-3}$ are the sediment and water density, respectively, g is the gravitational acceleration and D50 is the median grain size of the sediment. τ is the bed shear stress magnitude, with the subscript x referring to either currents (c) or waves (w):

$$\tau_c = \frac{\rho_w g u_c^2}{18 \log \left(\frac{12h}{2.5D50} \right)^2} \quad (2)$$

and

$$\tau_w = 0.5 \rho_w f_w u_w^2 \quad (3)$$

In these equations, h is the water depth and u_c is the time- and depth-averaged current velocity. The friction coefficient f_w is

$$f_w = \exp \left[-5.977 + 5.213 \left(\frac{A_\delta}{2.5D50} \right)^{-0.194} \right] \quad (4)$$

in which A_δ is the near-bed orbital excursion according to linear theory:

$$A_\delta = \frac{u_w T_{m-10}}{2\pi} \quad (5)$$

Ripple height predictors

Since predictors are commonly used to assess ripple characteristics and bed roughness, which are in turn used to calculate sediment transport, it is important to know how well they perform. According to Van Rijn and Havinga (1995), the bed roughness of small-scale ripples in natural conditions is equal to the ripple height. Therefore, some common ripple height predictors are chosen here. The predictor of van Rijn (2007) (called VR07 hereafter) is incorporated into the Delft3D model. Its inputs are the near-bed peak orbital velocity u_w , the depth-averaged current velocity u_c and the median grain size $D50$. Given the Ameland $D50$, the VR07 predicted ripple height η_p is

$$\eta_p = \begin{cases} 150 \times D50 & \text{if } \psi \leq 50 \\ (182.5 - 0.652 \times \psi) \times D50 & \text{if } 50 < \psi \leq 250 \\ 20 \times D50 & \text{if } \psi > 250 \end{cases} \quad (6)$$

in which total wave–current velocity $u_{wc} = \sqrt{u_w^2 + u_c^2}$ and mobility parameter $\psi = \frac{u_{wc}}{(s-1)gD50}$, with s the ratio of sediment density divided by water density and g the gravitational acceleration.

In TELEMAC, the Wiberg and Harris (1994) ripple model is used to calculate the wave-related ripple height in the wave–current dominated regime:

$$\eta_p = \alpha \times \begin{cases} 0.17 \times 0.62 D_0 & \text{if orbital ripples, } D_0/D50 < 2000 \\ 535 D50 \times \exp \left(-0.095 \left[\ln \left(\frac{D_0}{\eta_p} \right) \right]^2 + 0.442 \ln \left(\frac{D_0}{\eta_p} \right) - 2.28 \right) & \text{if anorbital ripples, } D_0/D50 > 5000 \end{cases} \quad (7)$$

in which near-bed orbital diameter $D_0 = H_s / \sinh(kh)$. Since η_p appears on both sides of Equation (7), this equation has to be solved iteratively. The correction factor α represents the effect of the current, according to Tanaka and Dang (1996) (TD96):

$$\alpha = 1 + 0.81 \times \left[\tanh \left(0.3 \times S_*^{2/3} \right) \right]^{2.5} \left(\frac{u_c}{u_w} \right)^{1.9} \quad (8)$$

in which dimensionless grain size S_* is given by

$$S_* = D50 \frac{\sqrt{(s-1)gD50}}{4\nu} \quad (9)$$

with ν being the kinematic viscosity of the fluid ($1.36 \times 10^{-6} \text{ m}^2 \text{ s}^{-1}$).

In the MIKE21 model, an adapted version of Nielsen (1979) (Ni79) is used to calculate ripple height. The inputs are near-bed orbital velocity u_w , amplitude of wave orbital motion A , water depth h , depth-averaged current velocity u_c and median grain size $D50$. The ripple height is given by

$$\eta_p = h_r \times R_f \times \frac{u_{fc}}{u_{fw}} \quad (10)$$

Here, h_r is the ripple height in pure wave motion, given by $h_r = 21 \psi_w^{-1.85} u_w$, in which ψ_w is the wave-related mobility parameter, $\psi_w = u_w^2 / [(s-1)gD50]$. R_f is a reduction factor:

$$R_f = \begin{cases} 1 & \text{for } \frac{u_{fc}}{u_{fw}} \leq 0.1 \\ 0.5 + 0.5 \cos \left[\left(\frac{u_{fc}}{u_{fw}} - 0.1 \right) \times \frac{\pi}{1.9} \right] & \text{for } 0.1 < \frac{u_{fc}}{u_{fw}} < 2 \\ 0 & \text{for } \frac{u_{fc}}{u_{fw}} \geq 2 \end{cases} \quad (11)$$

in which u_{fc} and u_{fw} are given by

$$u_{fc} = \frac{u_c}{6 + 2.5 \ln \left(\frac{h}{k_r + 2.5D50} \right)} \quad (12)$$

and

$$u_{fw} = \sqrt{0.5 f_w u_w^2} \quad (13)$$

with ripple roughness $k_r = (16h_r^2)/\lambda$, in which ripple wavelength $\lambda = h_r / (0.342 - 0.34(0.5f_w\psi_w)^{0.25})$. The friction factor f_w is calculated by $f_w = \exp(5.213 \left(\frac{2.5D50}{u_w} \right)^{0.194} - 5.997)$.

Khelifa and Ouellet (2000) (KhO00) was additionally chosen here, because it is similar to VR07 in the sense that it uses a combined wave–current velocity, but also considers the angle between waves and currents (β). In this case, u_{wc} is

$$u_{wc} = \left(\frac{u_w}{\pi} \right)^2 + u_c^2 + 2 \frac{u_w}{\pi} u_c \cos \beta \quad (14)$$

The ripple height in KhO00 is given by

$$\eta_p = 0.5 \sqrt{u_{wc}} [0.32 + 0.017 \ln(1 + \psi)^2 - 0.142 \ln(1 + \psi)] \quad (15)$$

The four predictors above are equilibrium height predictors, whereas Soulsby et al. (2012) (So12) incorporates the time-evolution aspect of the ripple height to account for the non-equilibrium time evolution of the ripple characteristics caused by time-varying hydrodynamics. To do so, So12 uses the same inputs as VR07, but adds wave height H , water

depth, wave period and a time step. Instead of determining the combined wave–current velocity, the predictor determines for each time step whether waves or currents are dominant, using the Shields parameters. The ripples are wave dominated if $\theta_w \geq \max(0.42\theta_c^{0.47}, 0.08)$, with θ_w and θ_c given by Equation (1). In this case, as long as θ_w exceeds the critical bed shear stress θ_{cr} , the equilibrium ripple length and height are based on $\Delta = A/D50$ and the rate of change is based on ψ_w . If the ripples are current dominated, equilibrium ripple length and height are based on $D50$ and the rate of change is based on θ_c and θ_{cr} . The actual ripple height is then calculated with a Runge–Kutta integration of the considered time step. For wave-generated ripples, the characteristic timescale is equal to one wave period (in accordance with Doucette and O'Donoghue, 2006), whereas for current-generated ripples this timescale depends on η , λ and $D50$. When the wave- or current related bed shear stress is below θ_{cr} , the ripples do not change and remain at the pre-existing value.

Even though all of the predictors mentioned above are used to predict bedform heights in various environmental conditions, most of them were created for specific settings. VR07 was based on field and flume studies with a large range of $D50$, and was tested for coastal applications using field data

with D_{50} of 0.300 mm. Although TD96 was developed specifically for lab conditions, TELEMAC also depends on Wiberg and Harris (1994), which was based on both field and lab conditions. Both predictors were made for grain sizes ranging from 0.1 to more than 0.65 mm. Ni79 was based on a flume study with D_{50} ranging from 0.08 to 0.36 mm. KhO00 was created based on a flume study, in which a large range of regular wave conditions were tested, with waves and currents travelling either perpendicularly or obliquely. Finally, the wave-related part of So12 was based on lab studies with $D_{50} = 0.44$ mm and regular, asymmetric waves. The current-related part was based on lab studies with $D_{50} = 0.095, 0.231, 0.237, 0.238$, and 0.510 mm. The predictor was tested against field and lab data, which were all coarser than 0.25 mm.

RESULTS

Observed hydrodynamics

To give an overview of the hydrodynamic conditions during the field campaign, Figures 4d–4g show the significant wave height, near-bed current speed, water depth and the angle between waves and currents at frame 4 through time. The tidal

range varied from 1 m during neap tide to 2 m during spring tide. The angle between waves and currents varied on the timescale of the tides; all values between 0 and 180° were measured. During fair-weather conditions significant wave heights were typically smaller than 1 m and maximum current speeds were 0.5 m s⁻¹. A storm with winds from the west occurred around 13 September (the maximum wave height was reached on 13 September at 13:30 h), with wave heights up to 3.5 m and near-bed current speeds of up to 1 m s⁻¹ in both the u (east) and v (north) direction at frame 4.

Although frame 1 was deployed during a different period, conditions were similar to those of frames 2–5. Wave heights were often between 1 and 2 m, with a maximum of 3.1 m and a minimum of 0.2 m. Current speeds in u and v directions were around 0.4 and 0.1 m s⁻¹, respectively, so they are a little smaller than those of frames 2–5.

Figure 5 shows the wave- and current-related bed shear stresses at all frames, both for the entire field campaign and for the storm and fair-weather periods that are indicated in Figure 4. Conditions are wave dominated if $\theta_w > \theta_c$ and current dominated if $\theta_c > \theta_w$. Wave-only and current-only conditions occur when $\theta_w > 0.2\theta_{c,cr}$ and $\theta_c > 0.2\theta_{w,cr}$, respectively (Kleinans, 2005). Figure 5a illustrates that conditions were mixed during most of the campaign at most of the frames.

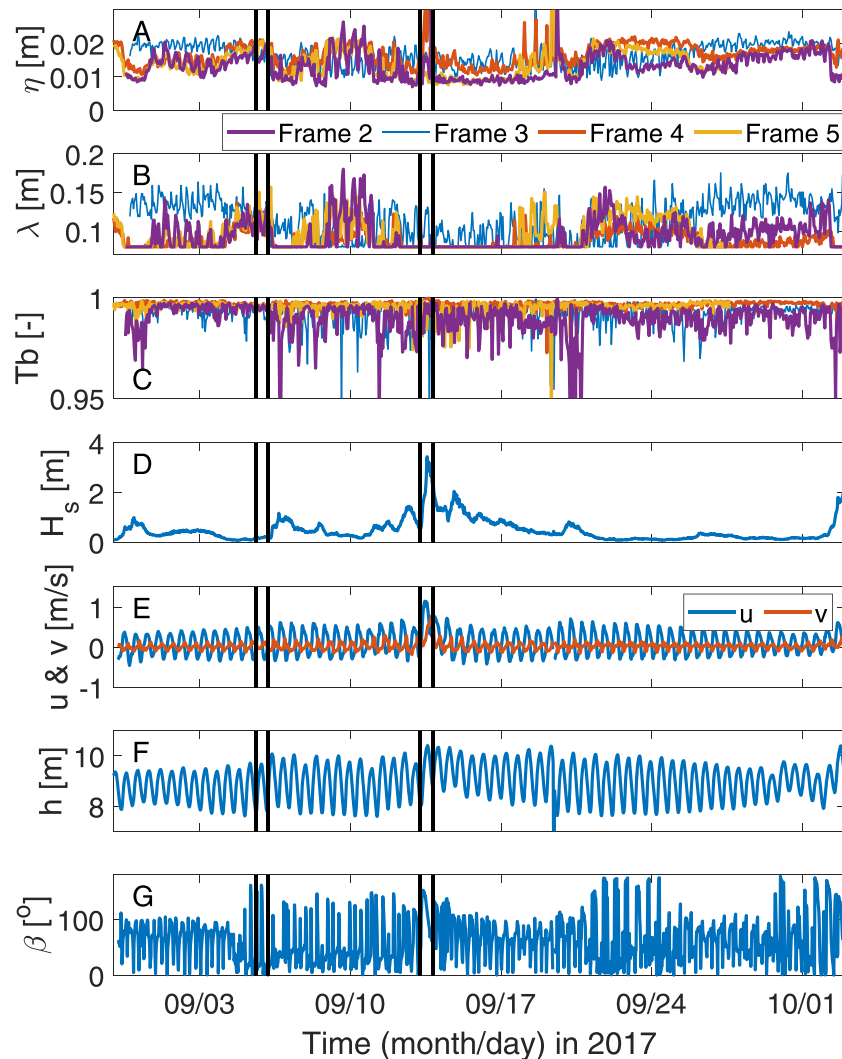


Figure 4. Time series of ripple heights η (A), lengths λ (B) and three-dimensionality Tb (C) for frames 2–5 and significant wave heights (D), current speeds (E), water depth (F) and angle between current vector and angle of wave propagation β (G) at frame 4 during the field campaign. Tb ranges between 0 and 1, with 1 indicating fully three-dimensional bedforms and 0 meaning fully two-dimensional bed forms. A representative calm-weather tidal cycle (5 September) and a storm tidal cycle (13 September) are indicated between black lines [Colour figure can be viewed at wileyonlinelibrary.com]

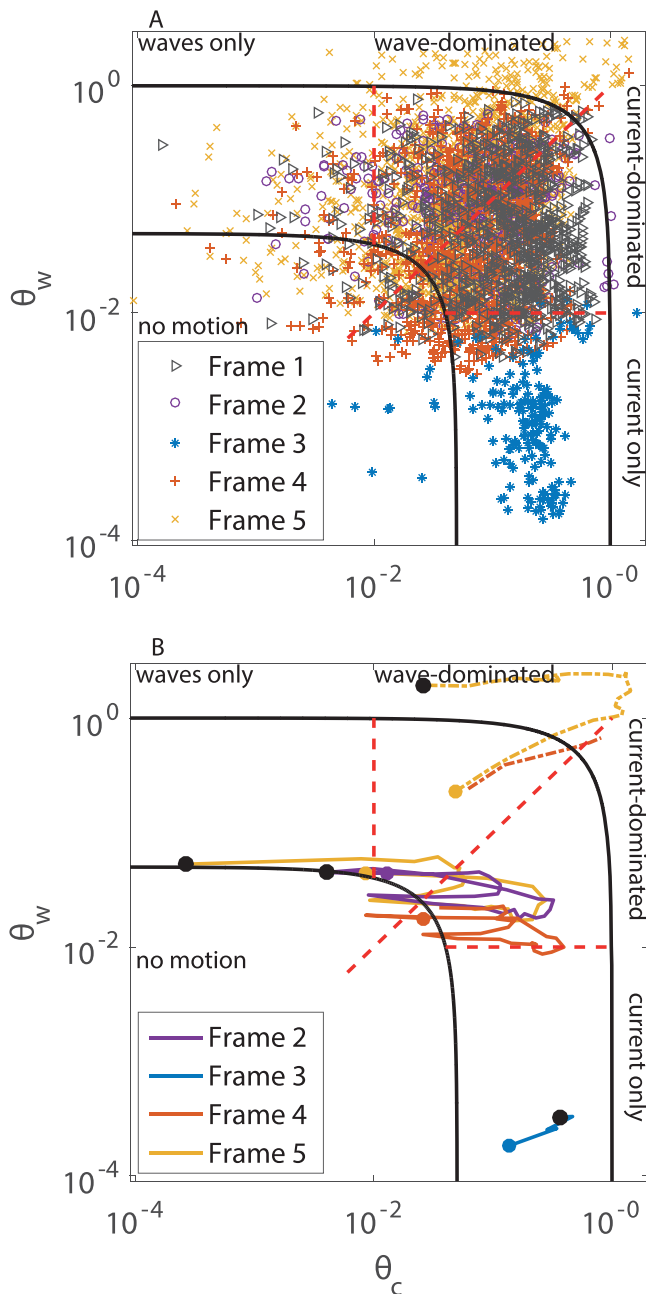


Figure 5. (A) Measured wave- versus current-related Shields stress for all frames. Black lines indicate sheet flow and incipient motion. Red dashed lines show the boundaries between regions of wave or current dominance, according to Kleinhans (2005). (B) Solid lines indicating calm periods and dash-dotted lines indicating storm periods that were introduced in Figure 4. The time series start at the coloured dots and end at the black dots [Colour figure can be viewed at wileyonlinelibrary.com]

Even frame 1, which was located offshore of the delta at 20 m depth and measured during a different period of time, shows wave-current-dominated conditions. Frames 2 and 5, which were placed on the delta lobes at 7 and 6 m water depth, show the largest spread, and also contain more wave-dominated conditions. Frame 3, which was located in the inlet, is the most distinct, with current-dominated conditions only.

During the storm, both wave and current shear stresses increased through time at frames 4 and 5, until the mobility exceeded the sheetflow criterion ($\theta_w + \theta_c > 1$ (Kleinhans, 2005)). After that, waves remained important for a longer period of time, while the current impact was already decreasing. At frame 2, the shear stresses were around the threshold of

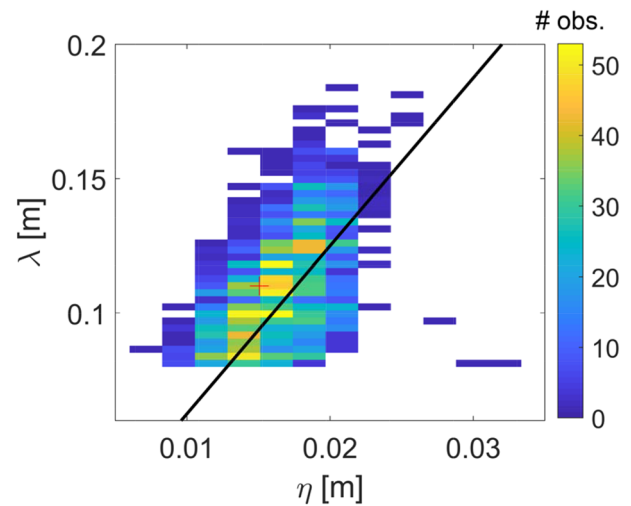


Figure 6. Two-dimensional histogram of ripple heights and lengths for all frames. The black line is the maximum equilibrium ripple steepness $\eta/\lambda = 0.16$. The average height and length are given by the red cross [Colour figure can be viewed at wileyonlinelibrary.com]

motion, but clearly induced by both waves and currents. During calm weather, frames 2, 4 and 5 were at or just below the threshold of motion until increasing current velocities (flood) caused an increase in current-related shear stress. During ebb, the current velocities decreased again, while the wave-related velocities remained constant, so the mobility decreased to near or below the threshold of motion again. The mobility at frame 3 was above this threshold for 84% of the time.

Observed ripple characteristics

As can be seen in Figures 4a–4c, the variations in ripple dimensions were relatively small in space and time. The patterns in η_m and λ through time were similar for frames 2, 4 and 5, with peaks in heights and lengths occurring simultaneously. Frame 3, which was located in the inlet, showed different patterns, although the range in η_m , λ and T_b were similar to those of the other frames. The average ripple height and length among all frames were 0.015 and 0.11 m, respectively (Figure 6). Despite the large ranges in θ_w , θ_c , H_s , u , v , h and β (Figures 5 and 4d–g), 79% of all observed ripples were between 0.01 and 0.02 m high and 83% were between 0.08 and 0.13 m long. On a timescale smaller than that of the tides, variability is found in η_m and λ , but most of the time these variations are smaller than the measurement accuracy. Around 10 September, clear peaks in height and length can be observed at frame 2, but during this period wave heights were low and current speeds were average.

On average, the ratio η/λ was 0.15. Most of the observed ripples were around the maximum equilibrium steepness of $\eta/\lambda = 0.16$, which was found by Wiberg and Harris (1994) and Camenen (2009), for example (Figure 6). Yet it is intriguing that this steepness was found for two-dimensional orbital vortex ripples, but the ones we observed were neither two-dimensional nor orbital. Given the small adaptation timescales we do expect the ripples to be in equilibrium for most of the time.

All ripples were highly three-dimensional; the T_b values ranged between 0.94 and 1, with the mean and median of the entire data set being 0.994 and 0.996, respectively (Figure 4c). Frames 4 and 5 show the highest T_b values (between 0.98 and 1), whereas those at frames 2 and 3 are a little lower (between 0.94 and 1). Visually, ripples appeared to be rela-

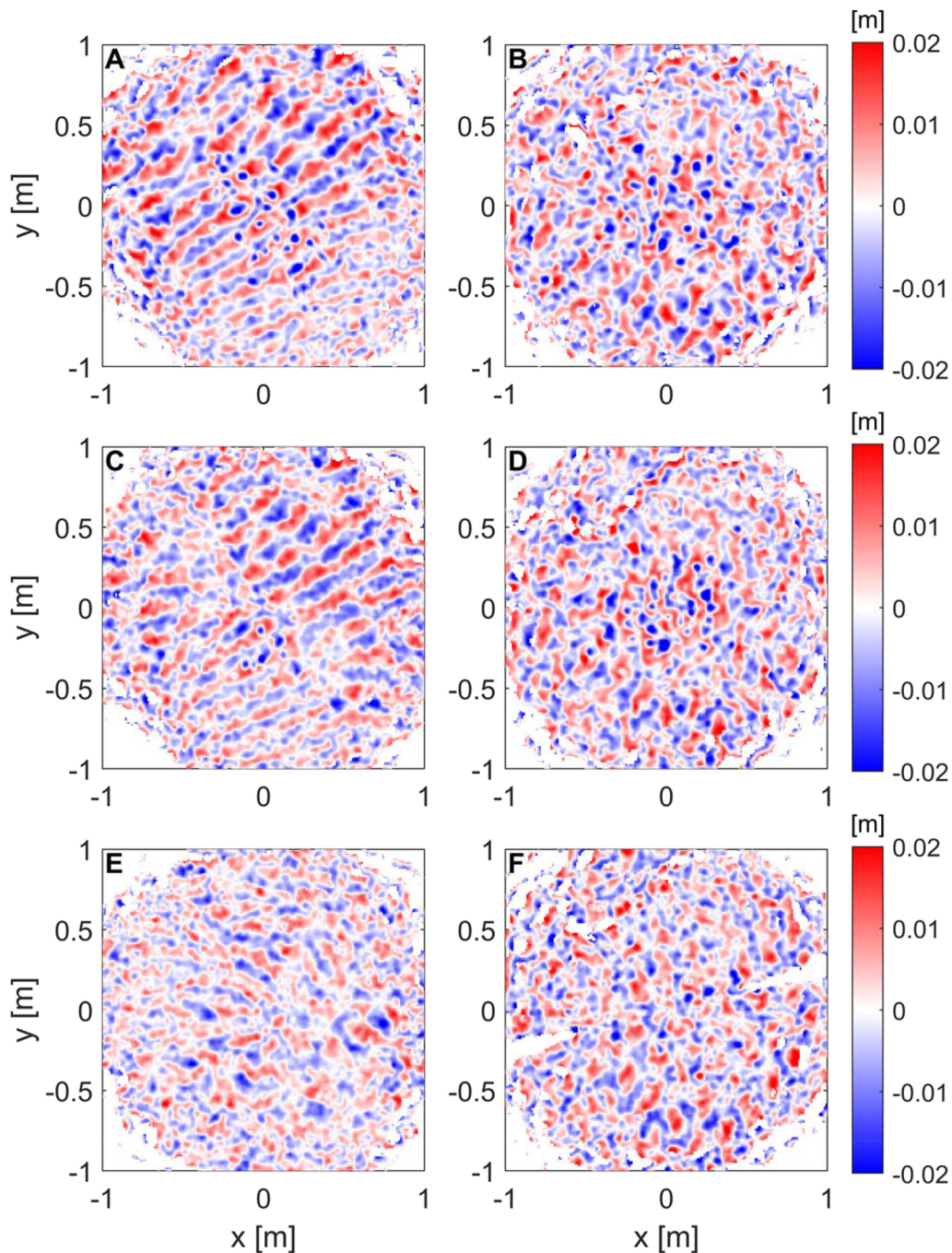


Figure 7. Examples of ripples found on the Ameland ebb-tidal delta. The ripples occurred at frame 3, 6 September 2017, 03:55 (A), 04:55 (C) and 05:55 (E) and at frame 4, 24 September 2017, 18:00 (B), 19:00 (D) and 20:00 (F) [Colour figure can be viewed at wileyonlinelibrary.com]

tively linear sometimes, for example after prolonged times of low waves. An example can be found in Figure 7c, which is representative of most of the images at frame 3, which was in a current-dominated regime (Figure 5). Yet the T_b value is still 0.984 here, because the standard deviations parallel and perpendicular to the ripple crests are both high. The ripples in Figure 7b have a T_b value of 0.986 and are representative for frames 1, 2, 4 and 5, which were in a wave–current-dominated regime (Figure 5). In all cases, the ripple field is changing frequently, although this does not lead to noteworthy variability in ripple length and height. Figure 7 shows that ripples migrate in some cases (Figure 7a vs. 7c), whereas their shape and orientation can also change significantly within an hour (Figure 7c vs. 7e). In this second case, individual ripples cannot be tracked through time.

Because the range in ripple heights, lengths and three-dimensionality is small, it is not surprising that relations between bedform characteristics and hydrodynamics (H_s , u_w , u_c , β , ψ , etc.) are generally absent. No statistically significant relation could be found between any of these hydrodynamic parameters and T_b and λ of the observed ripples; however, η_m was found to depend on the peak near-bed orbital velocity u_w ($r^2 = 0.38$ for a second-order polynomial fit) (Figure 8). There is a lot of scatter around the best fit line, but it is evident that the ripple height decreases when the orbital velocity increases. No such relation was found for the mean current velocity u_c , or for the ratio θ_c/θ_w . The ripples were not affected by the changes in megaripple characteristics either.

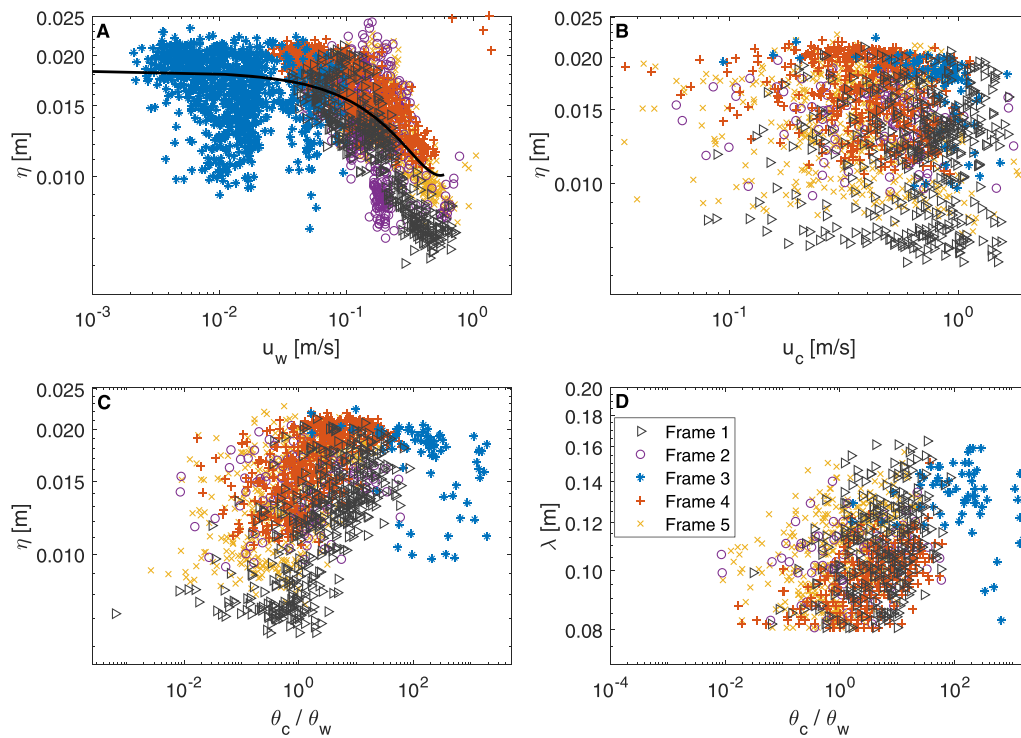


Figure 8. Relations between ripple characteristics and hydrodynamics for all five frame locations. (A) Ripple height η versus wave orbital velocity u_w . The line is the second order polynomial fit. (B) Ripple height η versus current velocity u_c . (C) Ripple height η versus ratio θ_c/θ_w . (D) Ripple length λ versus ratio θ_c/θ_w [Colour figure can be viewed at wileyonlinelibrary.com]

Bedform height predictors

The measured ripple heights (η_m) are now compared to those predicted (η_p) by the various predictors given before (Figure 9). As expected, all predictors are sensitive to either wave or current velocity, or both. Apart from Ni79, all predictors mainly overestimate the ripple height. Also, it was found that the ratio η_p/η_m for all predictors was similar for frames 2–5, while η_p/η_m was higher at frame 1. The So12 and VR07 predictors show similar results; they overpredicted ripple height in 96% and 97% of cases, respectively, and the ratio η_p/η_m is only sensitive to the wave orbital velocity. Especially with intermediate orbital velocities ($\sim 0.4 \text{ m s}^{-1}$) η_p is too high. For orbital velocities smaller than 0.2 m s^{-1} or around 0.8 m s^{-1} , η_p gets closer to η_m . Above 0.8 m s^{-1} , sheetflow conditions are predicted, in which the η_p decreases more than η_m . Overall, So12 works slightly better than VR07: 74% of the η_p are within a factor 2 (P2) of η_m , versus 60% for VR07.

The performance of KhO00 is related to the current velocity, and overpredicts most of the values. The P2 value is 10%, which is lower than all other predictors. The best predictions are found at very high ($u_c > 0.5 \text{ m/s}$) or very low ($u_c < 0.1 \text{ m s}^{-1}$) current velocities. Ni79 has the largest range in predicted ripple heights, and is both under- and overpredicting measured values. P2 is 23%. For TD96, P2 is a little higher, 33%, but it always overestimates η_p when $u_c > 0.3 \text{ m s}^{-1}$.

DISCUSSION

The ripple heights and lengths as found in the present study are small, yet they are always three to four times larger than the maximum footprint of the sonar. Scour occurred around the frames' legs, but no different characteristics were seen near the legs compared to directly under the 3D Profiling Sonar. Ripple heights, lengths and three-dimensionality are relatively constant, despite the large range in hydrodynamic conditions.

The hydrodynamic conditions observed here are compared to those of earlier studies in Figure 10. When this figure is compared to Figure 5a, it is visible that the present study is unique in the large range of hydrodynamic regimes that was studied; only in the present study were all types of regime found. Because of this large extent of data, some overlap can be found with the Shields parameters that were found in other studies as well. The study of Dolphin and Vincent (2009) is most comparable in terms of Shields numbers and grain size – their field site had a D_{50} of 0.220 mm – but they did not report actual bedform heights. However, they did find both two- and three-dimensional ripples, most of which (52%) were longer than 0.35 m . Thus their ripples were longer and more two-dimensional than those in the present study. Yet this difference is probably not caused by the forcing conditions, but by resolution issues: the images of Dolphin and Vincent (2009) had an accuracy of $\pm 0.02 \text{ m}$, so if small-scale ripples were present they would not have been visible in their study.

Wengrove *et al.*'s (2018) data are also comparable to our study in terms of Shields numbers, but they also found ripples that were more two-dimensional than in the present study. Also, the range in ripple heights and lengths was much larger than in the present study; Wengrove *et al.* (2018) found lengths of $0.14\text{--}2 \text{ m}$ and heights of up to 0.3 m . Both the different dimensions and three-dimensionality might be caused by the relatively fine sand on the Ameland ebb-tidal delta: the maximum grain size near the measurement frames was 0.226 mm . The study of Wengrove *et al.* (2018) was done in sand with 0.35 mm grain size. O'Donoghue *et al.* (2006) found that ripples become two-dimensional when the grain size is larger than 0.30 mm . They suggest that in sand with $D_{50} \leq 0.22 \text{ mm}$ the ripples can only become two-dimensional when the mobility (ψ) is very low. They explain this by the sand's susceptibility to turbulence: coarse grains will mainly react to the 'main' flow, which is two-dimensional, while finer sediment reacts to the small-scale three-dimensional turbulence in the flow. This implies that the bedform dimensions will

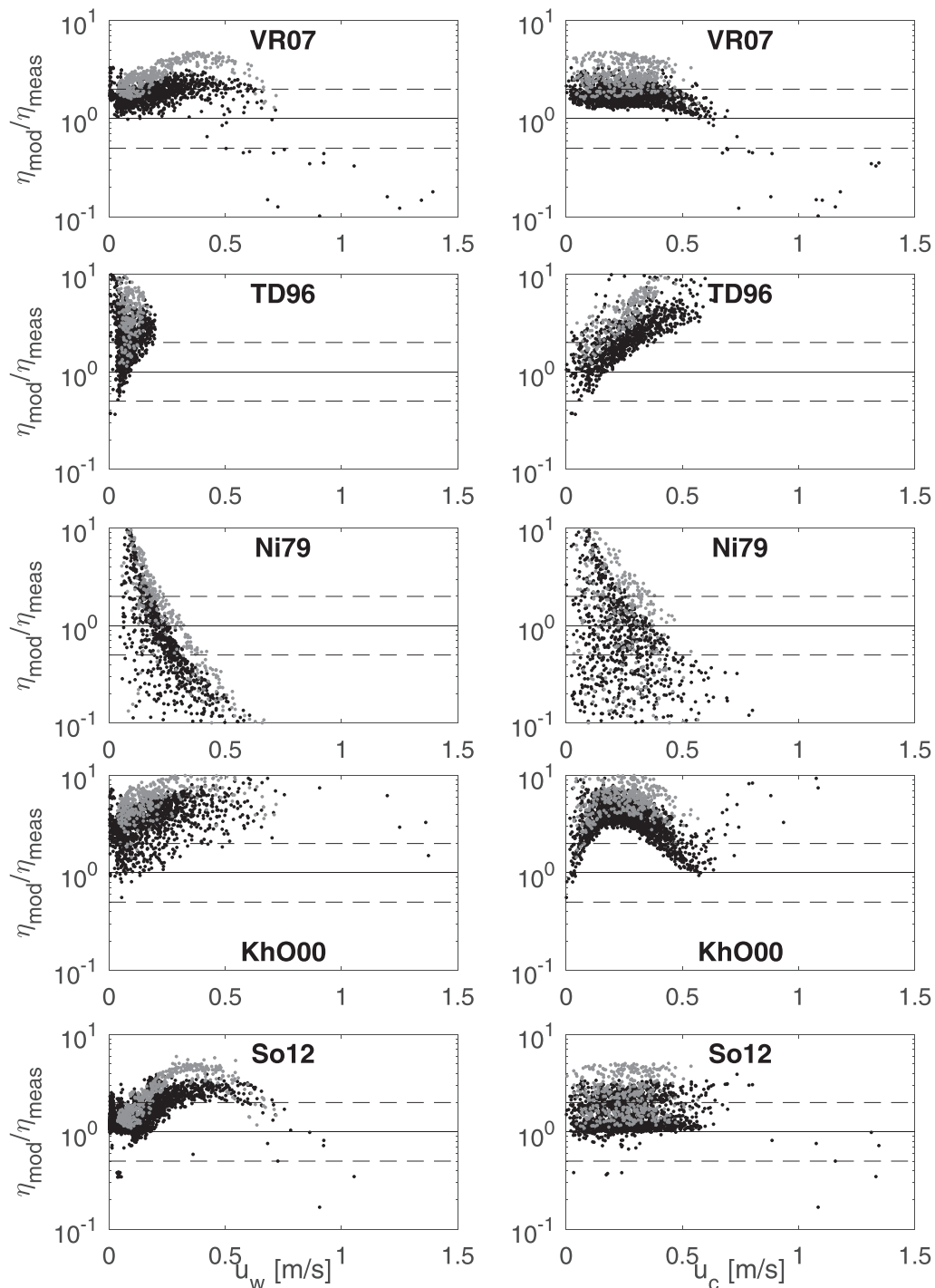


Figure 9. Ratio between predicted and measured ripple height, as a function of wave orbital velocity u_w (left column) and current velocity u_c (right column). Grey dots are data from frame 1, black dots are data from frames 2–5. These were plotted together because they were highly similar. The black line is the line of perfect agreement, and the dotted lines are ratios of 0.5 and 2. For clarity, y-axes were clipped at 0.1 and 10; therefore results outside this range are not shown. For TD96, the iterative equations could not be solved when $u_w > 0.2 \text{ m s}^{-1}$

not decrease further when D_{50} decreases below 0.22 mm, because they are only dependent on these small-scale hydrodynamics. This also explains why the ripples found in fine sediment are smaller than those in coarse sediment, which was also observed by O'Donoghue *et al.* (2006).

This hypothesis, linking fine-grained sand to small-scale three-dimensional turbulence, is further confirmed by the other studies presented in Figure 10. With sand having $D_{50} = 0.255 \text{ mm}$, the study of Bolaños *et al.* (2012) is more comparable to our study. They also found a smaller range in ripple dimensions than Wengrove *et al.* (2018): their height was generally between 0.02 and 0.04 m, with peak values of up to 0.17 m, and their wavelength was 0.2–0.3 m, with

peak values of 1.0 m. However, only two-dimensional profile measurements were done, so there is no information about three-dimensionality. The study of Krämer and Winter (2016) was done in a region with a small grain size of 0.105 mm, but also in an environment with low mobility (35 m water depth). Ripples were found to be three-dimensional, similar to those found in this study (Figure 7a), with heights of 0.015–0.02 m and a mean length of 0.215 m. This is further evidence that the ripple heights are probably independent of location in fine-grained sediment.

In our field study, ripple heights were only found to be related to orbital velocity, whereas most predictors are dependent on current velocity as well. Just like three-dimensionality,

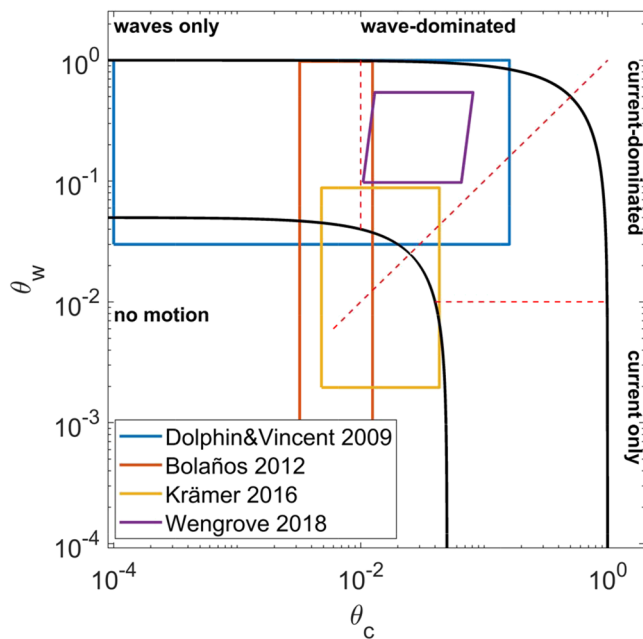


Figure 10. Shields diagram showing the range of Shields numbers found in previous studies [Colour figure can be viewed at wileyonlinelibrary.com]

the weak relation with hydrodynamics and the lack of variation in the bedform heights and lengths in the studied area might be caused by the small grain size. O'Donoghue *et al.* (2006) confirms that, because three-dimensional ripples are smaller than two-dimensional ripples, their dimensions are overpredicted by models. This is also found in the present study: most ripple heights are overpredicted by more than a factor of 2 by all five tested predictors. So12 and VR07 perform best, which is probably because they were tested for a wide range of field and flume conditions. On the other hand, they were only tested for cases with grain sizes larger than 0.25 mm. This could explain why they overpredict ripple heights in an environment with smaller grains. KhO00 incorporates the angle between waves and currents, but this parameter was found to have no effect on the ripple dimensions in the present study. Furthermore, this predictor was created based on a flume study, which, even though a large range of conditions were tested, was probably not representative of the field. This also holds for Ni79 and TD96. The incorporation of the time-evolution aspect of bedform height in So12 was expected to give this predictor a major advantage, but it was not a substantial improvement over VR07. Therefore, the higher P2 for So12 can only be ascribed to its formulation in general. This is because the adaptation timescales are too small to affect the equilibrium heights. Since the sonar measurements were done once per hour, the time lag effect is not visible in the results. Furthermore, most of the ripples were around the equilibrium steepness. According to Doucette and O'Donoghue (2006) and Soulsby *et al.* (2012), in wave-dominated situations the timescale is equal to a wave period, so 5–10 s, and in current-dominated situations it is computed from So12 to be roughly 7 min. These small timescales imply that they are not relevant on highly dynamic locations with only very small ripples such as ebb-tidal deltas. In short, the predictors are highly sensitive to both wave- and current-related velocities, while the measured ripples were found to depend only on wave orbital velocity. This implies that the prediction of ripple heights in fine sediment could be improved by using predictors that are only dependent on waves. Also, because most ripple heights and lengths are within a factor of 2 of the average, a constant value could be

used as well, in this case $\eta = 0.015$ m and $\lambda = 0.11$ m. By doing so, 97% of predictions are within a factor of 2 of the measurements (P2), which is higher than all predictors that were studied. Further research is necessary to find out whether this improves the sediment transport calculations as well.

CONCLUSIONS

Our data of the Ameland ebb-tidal delta show small wave–current ripples that are highly three-dimensional, and are on average 0.015 m high and 0.11 m long, despite strong variations in hydrodynamical conditions. The weak to non-existent dependence of ripple characteristics on hydrodynamics might be caused by the small grain size. The five tested ripple height predictors all overpredicted the measured ripple height in most cases. This is because they were not created for small grain sizes, and are highly dependent on current velocity, which was shown here not to be related to ripple height. Therefore, the use of constant ripple height and length values is more accurate than any of the predictors here. This could potentially also improve the prediction of sediment transport in wave–current-dominated environments with grain sizes smaller than 0.25 mm.

ACKNOWLEDGEMENTS

The authors thank everyone involved in the field campaign, especially Marcel van Maarseveen (UU), Henk Markies (UU), Jan-Willem Mol (Rijkswaterstaat) and the entire SEAWAD team. This project is part of the research program SEAWAD, a 'Collaboration Program Water' with project number 14489, which is financed by the Netherlands Organisation for Scientific Research (NWO) Domain Applied and Engineering Sciences, and co-financed by Rijkswaterstaat (Ministry of Infrastructure and Water Management in the Netherlands). The measurement campaign was co-financed by Rijkswaterstaat as well, in the context of the Coastal Genesis 2.0 project. The PhD project of LB is financed by the SEAWAD project. We thank the Special Issue editors, Knut Krämer and an anonymous reviewer for their constructive comments on the manuscript.

Conflicts of interest

The authors declare that there are no conflicts of interest.

Data availability statement

Research data will be made available through the Coastal Genesis 2.0 data portal: <https://waterinfo-extra.rws.nl/download-data/>

References

- Andersen K. H., Faraci C. 2003. The wave plus current flow over vortex ripples at an arbitrary angle. *Coastal Engineering* **47**(4): 431–441. [https://doi.org/10.1016/s0378-3839\(02\)00158-8](https://doi.org/10.1016/s0378-3839(02)00158-8).
- Ashley G. M. 1990. Classification of large-scale subaqueous bedforms: A new look at an old problem. *Journal of Sedimentary Research* **60**(1): 160–172.
- Bolaños R, Thorne P. D., Wolf J. 2012. Comparison of measurements and models of bed stress, bedforms and suspended sediments under combined currents and waves. *Coastal Engineering* **62**: 19–30. <https://doi.org/10.1016/j.coastaleng.2011.12.005>.

- Brakenhoff L. B., Ruessink B. G., van der Vegt M. 2019. Characteristics of saw-tooth bars on the ebb-tidal deltas of the Wadden Islands. *Ocean Dynamics* **69**: 1273–1285. <https://doi.org/10.1007/s10236-019-01315-w>.
- Buijsman M. C., Ridderinkhof H. 2008. Long-term evolution of sand waves in the Marsdiep inlet. I. High-resolution observations. *Continental Shelf Research* **28**: 1190–1201.
- Camenen B. 2009. Estimation of the wave-related ripple characteristics and induced bed shear stress. *Estuarine, Coastal and Shelf Science* **84**(4): 553–564. <https://doi.org/10.1016/j.ecss.2009.07.022>.
- Davis J. P., Walker D. J., Townsend M., Young I. R. 2004. Wave-formed sediment ripples: Transient analysis of ripple spectral development. *Journal of Geophysical Research* **109**(C7). <https://doi.org/10.1029/2004JC002307>.
- Deigaard R., Drønen N., Fredsøe J., Jensen J. H., Jørgensen MP. 1999. A morphological stability analysis for a long straight barred coast. *Coastal Engineering* **36**(3): 171–195. [https://doi.org/10.1016/s0378-3839\(99\)00005-8](https://doi.org/10.1016/s0378-3839(99)00005-8).
- Dolphin T., Vincent C. 2009. The influence of bed forms on reference concentration and suspension under waves and currents. *Continental Shelf Research* **29**(2): 424–432. <https://doi.org/10.1016/j.csr.2008.11.001>.
- Doucette J. S., O'Donoghue T. 2006. Response of sand ripples to change in oscillatory flow. *Sedimentology* **53**(3): 581–596. <https://doi.org/10.1111/j.1365-3091.2006.00774.x>.
- Elias E. P. L., Hansen J. E. 2013. Understanding processes controlling sediment transports at the mouth of a highly energetic inlet system (San Francisco Bay, CA). *Marine Geology* **345**: 207–220. <https://doi.org/10.1016/j.margeo.2012.07.003>.
- Elias E. P. L., van der Spek A. J. F., Wang Z. B., De Ronde J. 2012. Morphodynamic development and sediment budget of the Dutch Wadden Sea over the last century. *Netherlands Journal of Geosciences* **91**(3): 293–310.
- FitzGerald D. M. 1982. Sediment bypassing at mixed energy tidal inlets. *Coastal Engineering* **1**(18): 1094–1118.
- Florens E., Eiff O., Moulin F. 2013. Defining the roughness sublayer and its turbulence statistics. *Experiments in Fluids* **54**(4): Article no. 1500. <https://doi.org/10.1007/s00348-013-1500-z>.
- Grinsted A., Moore J. C., Jevrejeva S. 2004. Application of the cross wavelet transform and wavelet coherence to geophysical time series. *Nonlinear Processes in Geophysics* **11**(5/6): 561–566.
- Guo J. 2002. Simple and explicit solution of wave dispersion equation. *Coastal Engineering* **45**(2): 71–74.
- Herrling G., Winter C. 2014. Morphological and sedimentological response of a mixed-energy barrier island tidal inlet to storm and fair-weather conditions. *Earth Surface Dynamics* **2**(1): 363–382. <https://doi.org/10.5194/esurf-2-363-2014>.
- Hoekstra P., Bell P., van Santen P., Roode N., Levoy F., Whitehouse R. 2004. Bedform migration and bedload transport on an intertidal shoal. *Continental Shelf Research* **24**(11): 1249–1269. <https://doi.org/10.1016/j.csr.2004.03.006>.
- Israel C. G., Dunsbergen D. W. 1999. *Cyclic morphological development of the Ameland inlet, the Netherlands*, In Proceedings of the IAHR Symposium on River, Coastal and Estuarine Morphodynamics Department of Environmental Engineering, University of Genoa: Italy, 705–714.
- Jackson R. G. 1975. Hierarchical attributes and a unifying model of bed forms composed of cohesionless material and produced by shearing flow. *Geological Society of America Bulletin* **86**(11): 1523–1533.
- Khelifa A., Ouellet Y. 2000. Prediction of sand ripple geometry under waves and currents. *Journal of Waterway, Port, Coastal, and Ocean Engineering* **126**(1): 14–22.
- Kleinhans M. G. 2005. Phase diagrams of bed states in steady, unsteady, oscillatory and mixed flows. In *Sandpit: Sand Transport and Morphology of Offshore Sand Mining Pits*, van Rijn L. C., Soulsby R. L., Hoekstra P., Davies A. G. (eds), Aqua Publications: Los Angeles, CA, Paper Q.
- Kleinhans M. G., Grasmeijer B. T. 2006. Bed load transport on the shoreface by currents and waves. *Coastal Engineering* **53**: 983–996. <https://doi.org/10.1016/j.coastaleng.2006.06.009>.
- Krämer K., Winter C. 2016. Predicted ripple dimensions in relation to the precision of in situ measurements in the southern North Sea. *Ocean Science* **12**(6): 1221–1235. <https://doi.org/10.5194/os-12-1221-2016>.
- Lefebvre A., Ernsten V. B., Winter C. 2013. Estimation of roughness lengths and flow separation over compound bedforms in a natural-tidal inlet. *Continental Shelf Research* **61–62**: 98–111. <https://doi.org/10.1016/j.csr.2013.04.030>.
- Lefebvre A., Paarlberg A. J., Ernsten V. B., Winter C. 2014. Flow separation and roughness lengths over large bedforms in a tidal environment: A numerical investigation. *Continental Shelf Research* **91**: 57–69. <https://doi.org/10.1016/j.csr.2014.09.001>.
- Lenstra K. J. H., Pluis S. R. P. B., Ridderinkhof W., Ruessink B. G., van der Vegt M. 2019. Cyclic channel-shoal dynamics at the Ameland inlet: The impact on waves, tides, and sediment transport. *Ocean Dynamics* **69**(4): 409–425. <https://doi.org/10.1007/s10236-019-01249-3>.
- Li M. Z., Amos C. L. 1999. Field observations of bedforms and sediment transport thresholds of fine sand under combined waves and currents. *Marine Geology* **158**(1–4): 147–160.
- McCann D., Davies A., Bennell J. 2011. *Bed Roughness Feedback in TELEMAC-2D and SISYPHE*, In Proceedings of the XVIIIth Telemac and Mascaret User Club 2011. EDF R&D: Chatou, France, 99–104.
- Meirelles S., Henriquez M., Souza A. J., Horner-Devine A. R., Pietrzak J. D., Rijnsburger S., Stive M. J. F. 2016. Small scale bedform types off the South-Holland coast. *Journal of Coastal Research* **75**(sp1): 423–426. <https://doi.org/10.2112/si75-085.1>.
- Nayak A. R., Li C., Kiani B. T., Katz J. 2015. On the wave and current interaction with a rippled seabed in the coastal ocean bottom boundary layer. *Journal of Geophysical Research: Oceans* **120**(7): 4595–4624. <https://doi.org/10.1002/2014jc010606>.
- Nelson T. R., Voulgaris G. 2014. Temporal and spatial evolution of wave-induced ripple geometry: Regular versus irregular ripples. *Journal of Geophysical Research: Oceans* **119**(2): 664–688. <https://doi.org/10.1002/2013JC009020>.
- Nielsen P. 1979. *Some Basic Concepts of Wave Sediment Transport*. Doctoral Thesis, Institute of Hydrodynamics and Hydraulic Engineering Technical University of Denmark, Lyngby, Denmark.
- Núñez-González F., Hesse D., Ettmer B., Link O. 2014. Objective method for ranking bedforms with a 3-dimensionality-index. In *River Flow*, Schleiss A. J., De Cesare G., Franca M. J., Pfister M. (eds), Taylor & Francis: London; 1059–1065.
- O'Donoghue T., Doucette J. S., van der Werf J. J., Ribberink J. S. 2006. The dimensions of sand ripples in full-scale oscillatory flows. *Coastal Engineering* **53**(12): 997–1012. <https://doi.org/10.1016/j.coastaleng.2006.06.008>.
- Passchier S., Kleinhans M. G. 2005. Observations of sand waves, megaripples, and hummocks in the Dutch coastal area and their relation to currents and combined flow conditions. *Journal of Geophysical Research: Earth Surface* **110**(F04S15). <https://doi.org/10.1029/2004JF000215>.
- Pearson S. G., van Prooijen B. C., de Wit F. P., Meijer-Holzhauser H., de Looft A. P., Wang Z. B. 2019. Observations of suspended particle size distribution on an energetic ebb-tidal delta. In *Coastal Sediments 2019*, World Scientific: Singapore; 1991–2003, <https://doi.org/10.1142/978981120448700172>.
- Plant N. G., Holland K. T., Puleo J. A. 2002. Analysis of the scale of errors in nearshore bathymetric data. *Marine Geology* **191**(1–2): 71–86. [https://doi.org/10.1016/s0025-3227\(02\)00497-8](https://doi.org/10.1016/s0025-3227(02)00497-8).
- Ridderinkhof W., Hoekstra P., Van der Vegt M., De Swart H. E. 2016. Cyclic behaviour of sandy shoals on the ebb-tidal deltas of the Wadden Sea. *Continental Shelf Research* **115**: 14–26.
- Roskam A. P. Golfklimaten Voor De Nederlandse Kust, Technical Report Technical Report GWA0-88.046, Rijkswaterstaat, Tidal Waters Department The Hague, (in Dutch), 1988.
- Ruessink B. G., Brinkkemper J., Kleinhans M. G. 2015. Geometry of wave-formed orbital ripples in coarse sand. *Journal of Marine Science and Engineering* **3**(4): 1568–1594. <https://doi.org/10.3390/jmse3041568>.
- Sha L. P. 1989. Variation in ebb-delta morphologies along the West and East Frisian Islands, the Netherlands and Germany. *Marine Geology* **89**(1–2): 11–28.

- Smith J. D., McLean S. R. 1977. Spatially averaged flow over a wavy surface. *Journal of Geophysical Research* **82**(12): 1735–1746. <https://doi.org/10.1029/jc082i012p01735>.
- Soulsby R. L., Whitehouse R. J. S., Marten K. V. 2012. Prediction of time-evolving sand ripples in shelf seas. *Continental Shelf Research* **38**: 47–62. <https://doi.org/10.1016/j.csr.2012.02.016>.
- Tanaka H., Dang V. T. 1996. Geometry of sand ripples due to combined wave-current flows. *Journal of Waterway, Port, Coastal, and Ocean Engineering* **122**(6): 298–300. [https://doi.org/10.1061/\(asce\)0733-950x\(1996\)122:6\(298\)](https://doi.org/10.1061/(asce)0733-950x(1996)122:6(298)).
- Tanaka H., Shuto N. 1984. Sand movement due to wave-current combined motion. *Coastal Engineering in Japan* **27**(1): 179–191. <https://doi.org/10.1080/05785634.1984.11924386>.
- Tonnon P. K., van Rijn L. C., Walstra D. J. R. 2007. The morphodynamic modelling of tidal sand waves on the shoreface. *Coastal Engineering* **54**(4): 279–296. <https://doi.org/10.1016/j.coastaleng.2006.08.005>.
- Torrence C., Compo G. P. 1998. A practical guide to wavelet analysis. *Bulletin of the American Meteorological Society* **79**(1): 61–78.
- Traykovski P. 2007. Observations of wave orbital scale ripples and a nonequilibrium time-dependent model. *Journal of Geophysical Research* **112**(C6). <https://doi.org/10.1029/2006JC003811>.
- van der Vegt M., Mol J. W., Kok F., Holzhauer H., van der Werf J. J., Vermaas T., et al. 2020. Measurements of hydrodynamics, sediment, morphology and benthos on Ameland ebb-tidal delta and lower shoreface. *Under review with Earth System Science Data*.
- van Rijn L. C. 2007. Unified view of sediment transport by currents and waves. I. Initiation of motion, bed roughness, and bed-load transport. *Journal of Hydraulic Engineering* **133**(6): 649–667. [https://doi.org/10.1061/\(ASCE\)0733-9429\(2007\)133:6\(649\)](https://doi.org/10.1061/(ASCE)0733-9429(2007)133:6(649)).
- Van Rijn L. C., Havinga F. J. 1995. Transport of fine sands by currents and waves. II. *Journal of Waterway, Port, Coastal, and Ocean Engineering* **121**(2): 123–133.
- Wengrove M. E., Foster D. L., Lippmann T. C., de Schipper M. A., Calantoni J. 2018. Observations of time-dependent bedform transformation in combined wave-current flows. *Journal of Geophysical Research: Oceans* **123**(10): 7581–7598. <https://doi.org/10.1029/2018jc014357>.
- Wiberg P. L., Harris C. K. 1994. Ripple geometry in wave-dominated environments. *Journal of Geophysical Research: Oceans* **99**(C1): 775–789.
- Wu X., Parsons D. R. 2019. Field investigation of bedform morphodynamics under combined flow. *Geomorphology* **339**: 19–30. <https://doi.org/10.1016/j.geomorph.2019.04.028>.